# Ferromagnetic FeCo nanoparticles for biotechnology

Andreas Hütten[a],[*], Daniela Sudfeld[a], Inga Ennen[a], Günter Reiss[a],
Klaus Wojczykowski[b], Peter Jutzi[b]

[a]*Thin Films and Nanostructures, Faculty of Physics, University of Bielefeld, Universitaetsstr.25, D-33615 Bielefeld, Germany*
[b]*Inorganic Chemistry III, Faculty of Chemistry, University of Bielefeld, Universitaetsstr. 25, D-33615 Bielefeld, Germany*

Available online 3 March 2005

## Abstract

Calculated magnetophoretic mobility of a variety of magnetic compounds has identified FeCo to be an alternative for magnetite in in vitro biological cell separations. The synthesis of FeCo nanoparticles and the resulting microstructure is discussed as a function of the particle size. Their synthesis kinetics is modeled using a consecutive decomposition and growth model and is compared to experimental data.
© 2005 Published by Elsevier B.V.

## 1. Introduction

Paramagnetic carriers, ranging from microsized particles to nanosized colloids, which are linked to antibodies enable highly specified biological in vitro cell separations as well as therapeutic in vivo applications [1] such as drug-targeting, cancer therapy, lymph node imaging or hyperthermia. Ensuring biocompatibility and non-toxicity so as to meet the requirements for these applications, iron oxide-based particles, e.g. magnetite, are commonly used as the magnetically responsive component of commercially available magnetic microspheres. With the colloidal synthesis of superparamagnetic or ferromagnetic Co and FePt nanocrystals with superior magnetic moments [2–6], the question arises whether these nano-magnets could replace the iron oxide particles as magnetic carriers in in vitro separation and therapeutic in vivo technology. The magnetic potential of these nanocrystals can directly be evaluated, comparing their magnetophoretic mobility under identical experimental conditions.

*Corresponding author. Tel.: + 49 521 106 5420;
fax: + 49 521 106 6046.
*E-mail address:* huetten@physik.uni-bielefeld.de
(A. Hütten).

Besides their superior magnetic properties, their potential toxicity for in vivo applications has yet to be explored. However, the objective of this paper is to discuss aspects of the synthesis and the resulting micro-structure of FeCo nanoparticles. In addition it will shown that the composition of FeCo particles can be predicted as a function of the particle size employing a consecutive decomposition and growth model and is compared to measured data.

## 2. Theoretical evaluation of the magnetophoretic mobility of magnetic nanoparticles

In a simple model [7], the magnetophoretic mobility $\mu_m$ of a magnetic nanoparticle is derived for spherical magnetic carrier slowly moving in a liquid medium under the influence of an applied inhomogeneous magnetic field. Ignoring the forces due to gravity and buoyancy, the balance between the magnetic force acting on the magnetic carrier and the opposing hydrodynamic drag force exposed by the liquid medium yields $\mu_m$ as

$$\mu_m = \frac{(\chi_{carrier} - \chi_{medium})D_{carrier}^2}{18 \cdot \eta_{medium}}, \quad (1)$$

where $\mu_m$ depends on the viscosity $\eta_{medium}$ of the liquid medium, the carrier diameter $D_{carrier}$ and the effective susceptibility given by the difference in magnetic susceptibility between the carrier $\chi_{carrier}$ and the suspending medium $\chi_{medium}$. Thus, the carrier material-related parameters are $D_{carrier}$ and $\chi_{carrier}$. The latter quantity strongly depends on the magnetization of the magnetic carrier, the carrier size and the corresponding type of magnetization reversal and will be derived in the following. Fig. 1 compares the saturation magnetization at room temperature (RT) of the magnetic phases which are under consideration here. In addition, Fig. 1 summarizes the critical magnetic lengths of the superparamagnetic as well as the ferromagnetic single domain regime of spherical carriers hypothetically made of these phases. If $D_{carrier}$ is below the critical length for superparamagnetic behavior, then $\chi_{carrier}$ can be calculated using the
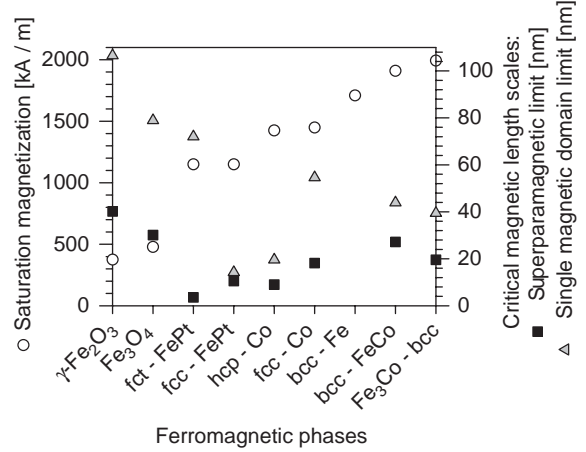


Fig. 1. Magnetization (open circles) of the ferromagnetic phases used in the calculation together with their superparamagnetic limit (black squares) and their single domain limit (grey triangles).

superparamagnetic susceptibility $\chi_{spm}$ [8] at RT or above:

$$\chi_{carrier}(T \geqslant RT)$$
$$= \chi_{spm} = \frac{\mu_0 M_{s,carrier}^2[(4/3)\pi(D_{carrier}/2)^3]}{3k_B T}. \quad (2)$$

Inserting this equation into Eq. (1) and neglecting the magnetic susceptibility of the liquid medium for simplification, $\mu_m$ is then given by

$$\mu_m(T \geqslant RT) = \frac{\pi\mu_0 M_{s,carrier}^2 D_{carrier}^5}{324 k_B T \eta_{medium}}. \quad (3)$$

The value of the magnetic field constant $\mu_0$ is given by $4\pi \times 10^{-7}$ Tm/A and $M_{s,carrier}$ denotes the saturation magnetization of the carrier material, see Fig. 1. Eq. (3) represents a tool which can be used to compare different carrier materials of otherwise identical morphologies moving in the same liquid medium. Hence, it can be concluded that the highest magnetophoretic mobility to be achieved, obviously requires the use of a carrier material with a large saturation magnetization. A comparison of a variety of ferromagnetic phases within the superparamagnetic regime is summarized in Fig. 2. The magnetophoretic mobility of $Fe_{50}Co_{50}$ and $Fe_{75}Co_{25}$ exceed that of the two iron
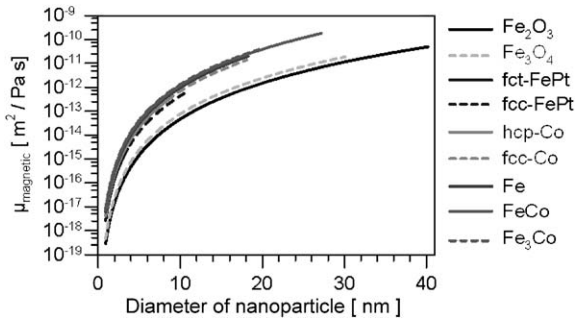
Fig. 2. Comparison of the calculated magnetophoretic mobility of different superparamagnetic nanoparticles at room temperature in water using Eq. (3). The relationships between the magnetophoretic mobility and the nanoparticle diameter is calculated over the whole superparamagnetic regime for each magnetic phase.

oxides by more than one order of magnitude over the whole diameter range. This result has a huge impact on the total number of nano-carriers which are needed and bound as magnetic labels to the surface of a biological cell so as to move this resulting magnetic microsphere (MCS) through a given liquid medium. The magneto-phoretic mobility for this case can similarly be derived for the superparamagnetic regime and is obtained as

$$\mu_{\mathrm{m}}(T \geqslant \mathrm{RT}) = \frac{\pi^2 \mu_0 \alpha \beta M_{\mathrm{s,carrier}}^2 D_{\mathrm{carrier}}^6 D_{\mathrm{MCS}}}{324 k_{\mathrm{B}} T \eta_{\mathrm{medium}}}. \qquad (4)$$

Here, $\alpha$ is the areal density of binding sites where a magnetic carrier can be bound to the biological cell surface and $\beta$ the number of magnetic carriers per binding site. $D_{\mathrm{MCS}}$ denotes the diameter of the microsphere. Eq. (4) allows for the evaluation of the magnetophoretic mobility of different MCSs under specific assumptions on their size, the suspending medium, its temperature and the ferromagnetic phase of the magnetic carrier in use. Assuming the same magnetophore-tic mobility for two MCSs of identical mor-phology moving in the same medium at the same temperature, but propelled by equally sized magnetic carriers made of different magnetic materials, Eq. (4) can also be used to derive the relation between the corresponding $\alpha_i$-values for

each MCS:

$$\frac{\mu_{\mathrm{m}}(\mathrm{MCS}\ 1, T \geqslant \mathrm{RT})}{\mu_{\mathrm{m}}(\mathrm{MCS}\ 2, T \geqslant \mathrm{RT})} = 1$$

$$\underset{\mathrm{rearranging}\ (4)}{\overset{\mathrm{with}\ \beta=1}{\longrightarrow}} \alpha_{\mathrm{MCS}\ 1} = \frac{M_{\mathrm{s,carrier\ on\ MCS}\ 2}^2}{M_{\mathrm{s,carrier\ on\ MCS}\ 1}^2} \alpha_{\mathrm{MCS}\ 2}. \tag{5}$$

Using $Fe_{50}Co_{50}$ and $Fe_3O_4$ as the magnetic materials for comparison, it turns out that the ratio of $\alpha_{\mathrm{MCS}\ 1}$ ($Fe_{50}Co_{50}$):$\alpha_{\mathrm{MCS}\ 2}$ ($Fe_3O_4$) is about 1:25. This means that 25 times more $Fe_3O_4$-than $Fe_{50}Co_{50}$-carriers of the same size are needed to provide the same magnetophoretic mobility for a MCS. As a consequence, magnetic microspheres equipped with $Fe_{50}Co_{50}$-nanocarriers can be made much smaller than commonly used ones and could reduce the risk of tissue irritation or embolizing small capillaries in drug-targeting technology.

This situation will also not change in the ferromagnetic single domain region, where the diameter of these nanocarriers exceeds the critical length for superparamagnetic behavior. In this case, the initial susceptibility is determined by the coherent rotation of the magnetization in the individual nanocarriers. Assuming that their easy axes are randomly distributed, then the resulting magnetophoretic mobility for ferromagnetic single domain nanocarriers is calculated to be

$$\mu_{\mathrm{m}}(T = \mathrm{RT}, K_1 > 0) = \frac{J_{\mathrm{s,carrier}}^2 D_{\mathrm{carrier}}^2}{54 \mu_0 K_1 \eta_{\mathrm{medium}}} \quad \mathrm{or}$$

$$\mu_{\mathrm{m}}(T = \mathrm{RT}, K_1 < 0) = \frac{J_{\mathrm{s,carrier}}^2 D_{\mathrm{carrier}}^2}{36 \mu_0 K_1 \eta_{\mathrm{medium}}}, \tag{6}$$

depending whether the magnetocrystalline aniso-tropy energy density $K_1$ at room temperature is positive or negative. $J_{\mathrm{s}}$ is the saturation polariza-tion and can be calculated by $J_{\mathrm{S}} = \mu_0 M_{\mathrm{S}}$. The comparison of the magnetophoretic mobility of different magnetic materials, which is shown in Fig. 3, reveals that the $Fe_{50}Co_{50}$ composition is superior even in the ferromagnetic single domain regime. The rather limited range of the single domain state of $Fe_{50}Co_{50}$ can be extended if it can experimentally be managed to order this phase so as to drive its magnetocrystalline anisotropy constant towards zero [9]. In that case, the
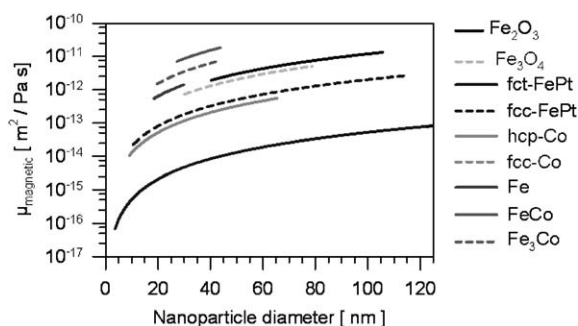
Fig. 3. Comparison of the calculated magnetophoretic mobility of different single domain nanoparticles at room temperature in water using Eq. (6). The relationships between the magnetophoretic mobility and the nanoparticle diameter is calculated up to 125 nm.

superparamagnetic regime of $Fe_{50}Co_{50}$ can be extended to much larger nanoparticle sizes.

Materials characterized by a large $K_1$, such as $Fe_{50}Pt_{50}$, exhibit a much smaller magnetophoretic mobility as compared to the iron oxides.

## 3. Experimental procedure

To synthesize FeCo-alloyed nanoparticles, two precursors, dicobaltoctacarbonyl $Co_2(CO)_8$ and ironpentacarbonyl $Fe(CO)_5$, have been used. Aiming for the $Fe_{50}Co_{50}$ composition, in a typical experiment with a Fe to Co ratio of 50:50, a solution of 0.25 g $Co_2(CO)_8$ and 0.2 mL $Fe(CO)_5$ dissolved in 3 mL 1,2-dichlorobenzene is injected into a vigorously stirred, refluxing solution of 0.1 g tri-*n*-octyl-phosphine oxide and 0.2 mL of oleic acid dissolved in 12 mL of 1,2-dichlorobenzene. All steps within this preparation procedure have been carried out under standard airless conditions. After cooling down to RT, the resulting solution is ferrofluid and can be further investigated. For microstructural characterization small portions of this ferrofluid can simply be dropped onto transmission electron microscopy (TEM) grids or deposited onto other appropriate substrates to allow the self-assembling of the isolated nanoparticles, each covered by an organic ligand shell, into monolayered superlattices. Details concerning the microstructural analysis are reported elsewhere [10].

The decomposition of the carbonyls has been measured with Fourier Transform Infra Red Spectroscopy (FT-IR) and the resulting decomposition rates were used as input parameters for LaMer's model [11] describing the growth kinetic of the alloyed FeCo, see below. These FT-IR experiments have been performed employing a Bruker Vector 22 FT-IR spectrometer with a NaCl chamber, allowing the observation of the complete wavelength spectrum in very short time intervals. It is also possible to measure the colloidal solution itself and to determine both the surfactants and the decomposition of the metal carbonyl precursors at different reaction times and temperatures. Consequently, the decomposition rate of the metal organic precursors can directly be determined.

## 4. Kinetic model of the formation of binary alloyed nanoparticles

Since the preparation of alloyed FeCo nanoparticles initially uses two precursors with different decomposition rates, the question is how to control their composition. Our approach to gain insights into the chemical reaction path is twofold. Firstly, the precursor decomposition rates have been determined via FT-IR and are used as input parameters for an extended LaMer model predicting the nucleation and growth kinetics of the nanoparticles. Secondly, the composition of FeCo nanoparticles after preparation is monitored as a function of particle size employing energy dispersive X-ray spectroscopy (EDX) in the nanoprobe mode. The comparison between prediction and measurement then will allow concluding on the reaction kinetics. For this purpose, LaMer's model has been extended to be able to treat the simultaneous decomposition of two precursors. The concept of this model is based on two consecutive reactions. The first reaction involves the simultaneous decomposition of two precursors [A] and [B]. These reactions are irreversible and of first order characterized by the corresponding decomposition rates $k_1$ and $k_2$.

Both reaction products, e.g. the free metallic A- or B-atoms, are monomers [C] with equal probability to serve as initial building blocks for

the final nanoparticle formation $[D]$ following another first-order reaction. In order to provide a steady state reaction, the corresponding nanoparticle formation rate $k_3$ is assumed to be significantly larger than the precursor decomposition rates. The resulting rate equations can be formulated as

$$\frac{d[A]}{dt} = -k_1[A] \tag{7}$$

$$\frac{d[B]}{dt} = -k_2[B] \tag{8}$$

Eqs. (7) and (8) can be solved independently (10, 11). An analogous rate equation for the monomers $[C]$ can also be found:

$$\frac{d[C]}{dt} = k_1[A] + k_2[B] - k_3[C], \tag{9}$$

$$[A] = [A]_0 e^{-k_1 t}, \tag{10}$$

$$[B] = [B]_0 e^{-k_2 t}. \tag{11}$$

By inserting these results for $[A]$ and $[B]$ into Eq. (9), the solution of this differential equation is given by

$$[C] = -\frac{k_1[A]_0}{k_1 - k_3} e^{-k_1 t} - \frac{k_2[B]_0}{k_2 - k_3} e^{-k_2 t}$$
$$+ \frac{(k_1 k_2[A]_0 + k_1 k_2[B]_0 - k_1 k_3[A]_0 - k_2 k_3[A]_0)}{(k_1 - k_3)(k_2 - k_3)} e^{-k_3 t}. \tag{12}$$

Starting the complete reaction process at $t = 0$ with the initial precursor quantity being $[A]_0$ and $[B]_0$ the conservation of mass requires the validity of

$$[D] = [A]_0 + [B]_0 - [C] - [A] - [B]. \tag{13}$$

Hence, the nanoparticle growth rate is determined by $v(t)$:

$$v(t) = \frac{d[D]}{dt}. \tag{14}$$

In order to obtain a quantity $x$ which represents the ratio of A- to B-atoms among all monomers as a function of reaction time $t$, $x(t)$

can defined by

$$x(t) = \frac{\frac{d[A]}{dt}}{\frac{d[B]}{dt}} = \frac{k_1[A]}{k_2[B]}. \tag{15}$$

Then, the time-dependent fraction $a(t)$ and $b(t)$ of A- and B-atoms of all monomers can be calculated by

$$a(t) = 1 - b(t) \tag{16}$$

$$b(t) = \frac{1}{x(t) + 1}. \tag{17}$$

Finally, the individual growth rates of A- and B-atoms forming the nanoparticle $[D]$ are related to Eq. (14):

$$v_A(t) = a(t)v(t), \tag{18}$$

$$v_B(t) = b(t)v(t). \tag{19}$$

Choosing a time interval defined by a reaction start time $t_i$ and a reaction ending time $t_f$, the nanoparticle composition in terms of the number of A- and B-atoms can be calculated by integrating the individual growth rates:

$$n_A = \int_{t_i}^{t_f} v_A(t)\,dt, \tag{20}$$

$$n_B = \int_{t_i}^{t_f} v_B(t)\,dt, \tag{21}$$

$$\text{or} \quad n = n_A + n_B = \int_{t_i}^{t_f} v(t)\,dt. \tag{22}$$

Assuming the particle diameter to be proportional to the cubic root of the total number of atoms the nanoparticle composition can be calculated as a function of the particle size.

To understand the kinetics of the formation of $Fe_{50}Co_{50}$ nanoparticles, FT-IR absorption measurements were performed so as to determine the relevant decomposition rates. Fig. 4 shows a typical absorption spectra of the colloidal solution of $Fe_{50}Co_{50}$ nanoparticles dissolved in 1,2 dichlorobenzene in reference to $Co_4(CO)_{12}$ and $Co_2(CO)_8$ dissolved in hexane and $Fe(CO)_5$ solved in dichlorobenzene. Obviously, the measured spectrum does not fit to that of the initially used $Co_2(CO)_8$ precursor. Thus, it was concluded that
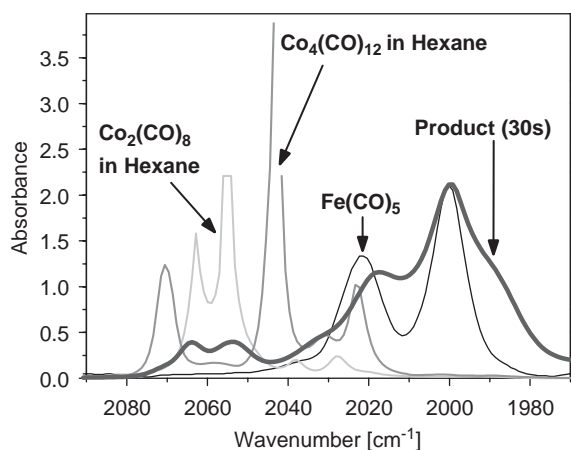
Fig. 4. Measured FT-IR absorbance spectra of the reaction product taken after a reaction time of 30 s. Also displayed are the relevant pure metal carbonyls solved in hexane which serve as references.
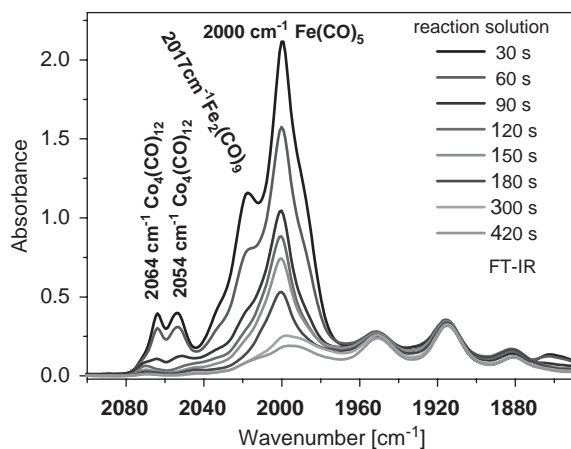


Fig. 5. FT-IR absorbance spectra of the time dependent decomposition of the involved metal carbonyl precursors during the formation process of FeCo alloyed nanoparticles.

$Co_2(CO)_8$ is not stable and is rapidly transformed to a more stable species. Such a precursor was identified as the tetra nuclear cobalt cluster $Co_4(CO)_{12}$. The corresponding transformation from $Co_2(CO)_8$ to $Co_4(CO)_{12}$ is extremely fast and already completed after 30 s of the total reaction time. A time resolved decomposition study as summarized in Fig. 5 confirms the presence of only three characteristic absorption

bands: $Fe(CO)_5$ at $2000\,cm^{-1}$, $Co_4(CO)_{12}$ at $2054\,cm^{-1}$ and at $2064\,cm^{-1}$. The Co source taking part in the reaction is consequently $Co_4(CO)_{12}$.
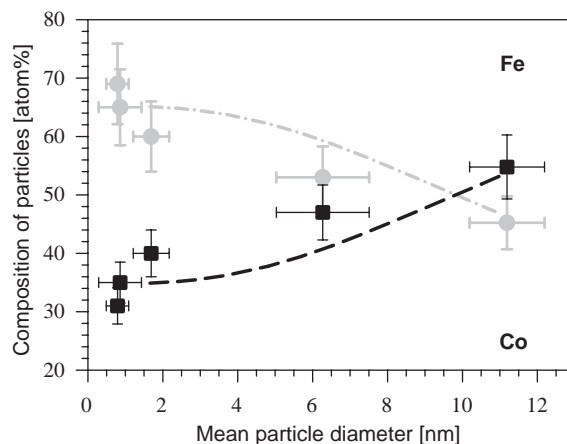


Fig. 6. Measured composition of the FeCo alloyed nanoparticles as a function of the mean particle diameter (solid circles). The fitting is based on the experimentally determined decomposition rates $k_1$ and $k_2$. $k_3$ was chosen as $0.1\,s^{-1}$. $k_1$, $k_2$ and $k_3$ were used as kinetic input data for the extended LaMer model which is displayed for the Fe- (dot-dashed line) and Co- (dashed line) concentration of the nanoparticles.
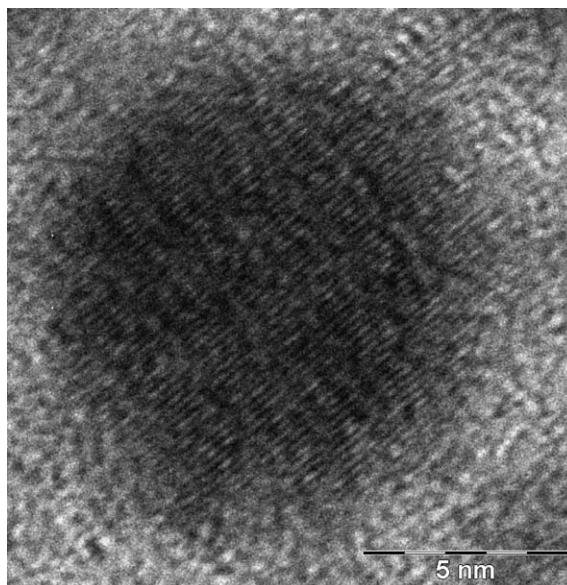


Fig. 7. HRTEM bright-field image of a single 11 nm sized BCC $Fe_{45}Co_{55}$ nanoparticle in (1 1 0) orientation.

Additionally, there is a small shoulder visible in the peak at $2017\,cm^{-1}$ belonging to $Fe_2(CO)_9$ which indicates that $Fe(CO)_5$ decomposes to a more stable precursor, diironnonacarbonyl, as well. The decomposition rates have been experi-mentally determined to be $k_1 = 7.52 \times 10^{-3}\,s^{-1}$ for $Fe(CO)_5$ and $k_2 = 1.36 \times 10^{-2}\,s^{-1}$ for $Co_4(CO)_{12}$. Hence, it can be concluded that the cobalt precursor decomposes about two times faster than the iron precursor.
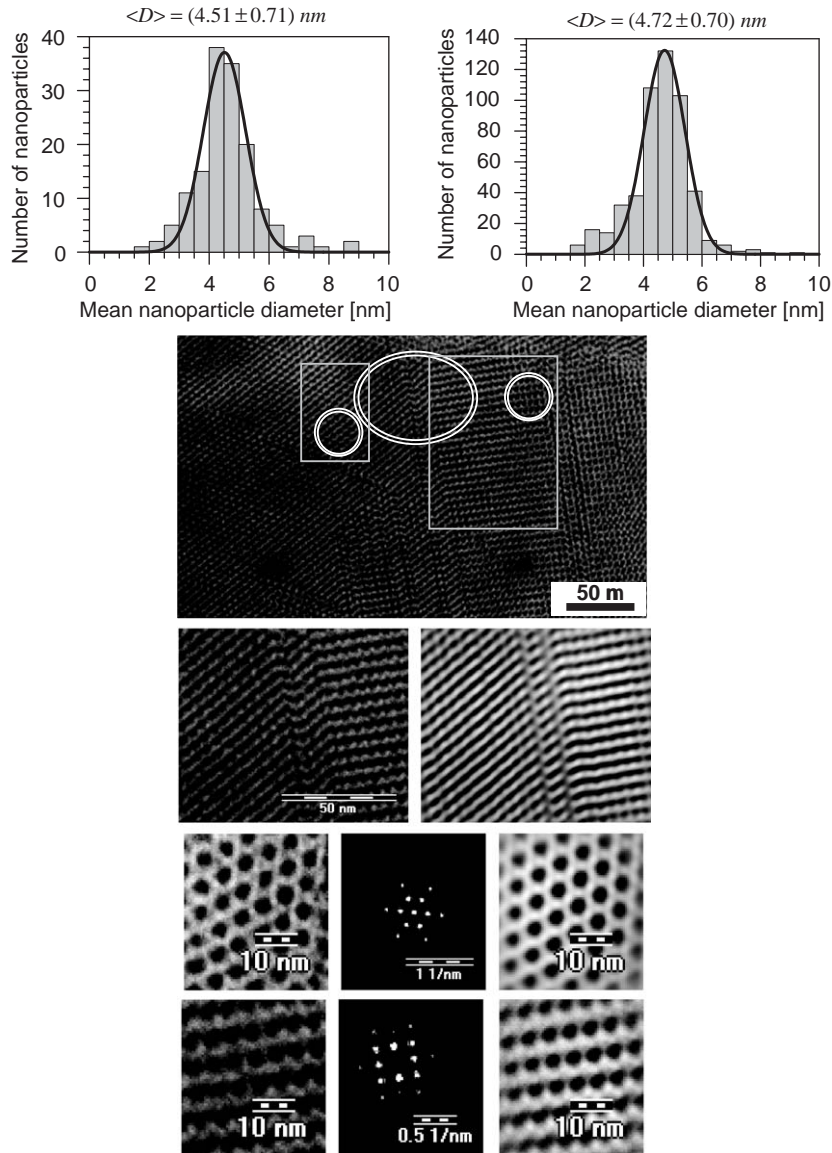


Fig. 8. Phase transformation in a $Fe_{55}Co_{45}$ superlattice from hexagonally ordered to cubic ordered regions each shown with FFT pattern and filtered FFT-image. The filtered images are taken from the doubled encircled areas. The size distributions shown on the top are the measured $Fe_{55}Co_{45}$ alloyed particles corresponding to the squared areas marked in the bright-field TEM image. The mean particle distance between the centers of two particles could be determined from the FFT-images and results in $\langle d \rangle = 4.8\,nm$ for the hexagonal region and $\langle d \rangle = 4.24\,nm$ for the cubic region.

High-resolution energy dispersive X-ray spectroscopy performed on $Fe_{50}Co_{50}$ self-assembled superlattices with different mean nanoparticle sizes revealed that their actual composition strongly depends on the particle diameter, as is shown in Fig. 6. This can be attributed to the slower decomposition of the $Fe(CO)_5$ precursor. Using the measured decomposition rates $k_1$ and $k_2$ of both precursors and choosing the nanoparticle formation rate to be $k_3 = 0.1\,s^{-1}$ as input parameters for the extended LaMer model, the experimentally determined dependence of the FeCo particle composition on their size can be verified fairly well, as is additionally be shown in Fig. 6.

The lattice parameter of a single $Fe_{45}Co_{55}$ nanoparticle was determined by analyzing the lattice fringes, see Fig. 7. The measured lattice plane distance is 0.193 nm and corresponds to the $(1\,1\,0)$ orientation of the BCC phase with a resulting lattice parameter of 0.2658 nm. This is in excellent agreement with the lattice constant for $Fe_{40}Co_{60}$ bulk material.

The formation of well-ordered 3D superlattices of FeCo nanoparticles can be taken as a hint for a very sharp particle size distribution as is shown in Fig. 8. Similar to the situation in solids, stacking faults can lead to hexagonal or cubic ordering regions in the 3D FeCo nanocrystals. The corresponding magnetization vs. field curve measured
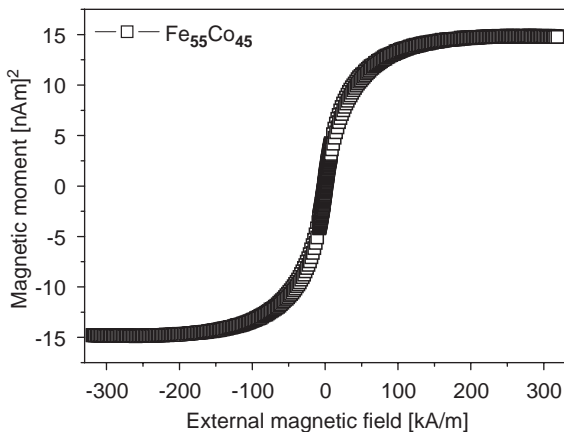
at room temperature of the 3D superlattice sample is given in Fig. 9. Although the individual FeCo nanoparticles are supposed to be superparamagnetic at room temperature because of their size, a small coercivity of 1.35 kA/m was detected. This can be attributed to magnetic interaction of adjacent closely packed FeCo nanocrystals.

## 5. Conclusions

We are able to synthesize superparamagnetic FeCo particles ranging from 1 to 11 nm. All nanocrystals are stabilized by an oleic acid ligand shell. Our magnetic analysis has revealed that $Fe_{50}Co_{50}$ nanoparticles are superior from the magnetophoretic mobility point of view. One important requirement for controlling their composition is the knowledge of decomposition kinetics of the precursor. This task is divided into two aspects as could be demonstrated. One is to identify the stable precursors. The other is to quantify the decomposition rates of the relevant precursors so as to gain insights into the kinetics. We have shown that an extended LaMer model can serve very well to predict the composition dependence of these FeCo nanoparticles on their size distribution. One further step to improve the $Fe_{50}Co_{50}$ nanocrystals is to work on the atomic ordering of each particle. This may be because the magnetocrystalline anisotropy constant decreases with increasing degree of atomic ordering. Consequently, the superparamagnetic limit would be shifted towards much larger particle sizes avoiding any magnetic induced agglomeration of the corresponding ferrofluid solutions. For the application of magnetic nanoparticles as markers in biological or biochemical systems, a suitable surrounding of the magnetic core has still to be realized. To create this link between magnetic particle and the molecule to probe is a task of the synthetic and analytical organic chemistry. The following requirements have to be fulfilled by the ligand molecules of the organic shell:

1. The bond between particle surface and polar ligand head group has to be tight enough to prevent a dynamic equilibrium with free ligands

Fig. 9. Corresponding magnetization loop of the self-assembled $Fe_{55}Co_{54}$ nanocrystals of Fig. 8.

in solution; i.e. a loss of the marker must be avoided. For this purpose oligomeric ligands could be used.

2. The ligand has to fit the geometry of the particle. Macromolecules like streptavidin are therefore inappropriate for particles in the lower nanometer range.

3. A flexible link between functionalized ligand and biomolecule has to provide a fast and uncomplicated detection.

Besides these properties concerning the probe function of the particle there are also some general requirements for ligands in nanoparticle systems: The organic shell has to stabilize the colloidal system during the synthetic steps and in the ready-to-use solutions. The ligands must therefore have a sufficiently long, flexible and non-polar chain and a geometry that allows a dense packing on the particle surface.

## References

[1] U. Häfeli, W. Schütt, J. Teller, et al. (Eds.), Scientific and Clinical Applications of Magnetic Carriers, Plenum, New York, 1997.

[2] C.B. Murray, S. Sun, W. Gaschler, et al., IBM J. Res. Dev. 45 (2001) 47.

[3] V.F. Puntes, K.M. Krishnan, A.P. Alivisatos, Science 291 (2001) 2115.

[4] D.P. Dinega, M.G. Bawendi, Angew. Chem. 111 (1999) 1906.

[5] S. Sun, C.B. Murray, H. Doyle, Mater. Res. Soc. Symp. Proc. 577 (1999) 385.

[6] S. Sun, C.B. Murray, D. Weller, et al., Science 287 (2000) 1989.

[7] J.J. Chalmers, Y. Zhao, M. Nakamura, et al., J. Magn. Magn. Mater. 194 (1999) 231.

[8] B.D. Cullity, Introduction to Magnetic Materials, Addison-Wesley Publishing Company, Reading, Massachusetts, 1972, p. 481.

[9] R.C. Hall, J. Appl. Phys. 30 (1959) 816.

[10] D. Sudfeld, I. Ennen, A. Hütten, et al., 2005 (this issue).

[11] V.K. LaMer, R.H. Dinegar, J. Am. Chem. Soc. 72 (1950) 4847.